Check for updates

Geophysical Research Letters®

RESEARCH LETTER
10.1029/2024GL111135

Key Points:

- New dense arrays covering Los Angeles basin enable better characterization of basin structure
- Sp converted phase provides an independent constraint on basin depth
- The deepest part of the central Los Angeles basin has an averaged depth of over 9 km

Supporting Information:

Supporting Information may be found in the online version of this article.

Correspondence to:
Y. Yang,
yanyang@caltech.edu

Citation:
Yang, Y., & Clayton, R. W. (2024). Mapping Los Angeles Basin depth with Sp converted phases. *Geophysical Research Letters*, *51*, e2024GL111135. https://doi.org/10.1029/2024GL111135

Received 2 JUL 2024
Accepted 8 SEP 2024

© 2024. The Author(s).
This is an open access article under the terms of the Creative Commons Attribution-NonCommercial-NoDerivs License, which permits use and distribution in any medium, provided the original work is properly cited, the use is non-commercial and no modifications or adaptations are made.

Mapping Los Angeles Basin Depth With Sp Converted Phases

Yan Yang[1] and **Robert W. Clayton**[1]

[1]Seismological Laboratory, California Institute of Technology, Pasadena, CA, USA

Abstract The depth of the Los Angeles (LA) basin is a critical factor for seismic hazard assessment and active tectonic studies. By analyzing S-waves generated by earthquakes below the basin that convert to P-waves at the sediment-bedrock interface, we estimate the maximum depth of the LA basin to be 9 km. This estimate depends on the velocities within and below the basin, and the depth presented here is based on the latest community velocity model. To map the basin depth, we use two dense arrays: the Community Seismic Network, a dense network of low-cost accelerometers in schools across LA region, and a basin-wide node survey conducted in 2022, consisting of about 300 geophones deployed for a month. Utilizing differential travel times between direct S and Sp converted phases of local earthquakes, we produce a detailed depth map of the LA basin.

Plain Language Summary A basin's depth influences how seismic waves resonate and amplify, affecting ground shaking during earthquakes. This information is vital for designing earthquake-resistant buildings and infrastructure in the densely populated Los Angeles area, which sits atop a sedimentary basin. We collected data from two dense seismic sensor arrays: the Community Seismic Network, which uses low-cost sensors placed in schools across the LA region, and a survey in 2022 using about 300 geophones deployed across the basin. By examining the travel times of seismic waves that convert at the sediment-bedrock interface, we provided an independent measure of the basin's depth with dense coverage. Our findings show that the deepest part of the central Los Angeles Basin reaches over 9 km.

1. Introduction

The Los Angeles (LA) basin was formed by the capture and subsequent rotation of the Transverse Ranges by the Pacific plate about 20 Ma ago. This created an accommodation space that became the LA basin and several other smaller basins. The basin has been modified by cycles of extension and compression events (Ingersoll & Rumelhart, 1999; Wright, 1991; Yerkes, 1965) and has been influenced by the presence of a complicate faulting including the Newport-Inglewood fault (NIF), which runs along the western edge of the basin (Hough & Graves, 2020; Shaw & Suppe, 1996). Sedimentary basins can trap and amplify earthquake ground shaking (Denolle et al., 2014; Kohler et al., 2020; Olsen, 2000), and given its location beneath the densely populated metropolitan area of Los Angeles, it is crucial to accurately characterize the structure of the LA basin for seismic hazard assessment. The resonant period of the basin, which is directly related to its depth, is particularly significant for the structural health and stability of high-rise buildings in the area. Despite its importance, the depth of the LA basin remains elusive, with current estimates of the depth based on gravity studies with poorly constrained densities (McCulloh, 1960). There is no basin-wide direct estimate of the basin depth.

The depth of the basin is also important for determining the basin stretching factor, which is the ratio of the preformation crustal thickness to the current one. The stretching factor provides insights into the tectonic processes that have shaped the basin over time, including the level of thermal subsidence and the extent of crustal thinning (Ma & Clayton, 2016; McKenzie, 1978; Turcotte & McAdoo, 1979). The basin is close to being in isostatic equilibrium, with the free-air gravity across the basin measured at −50 mgals. Without isostatic compensation, the gravitational response of the LA basin would be approximately −300 mgals (Turcotte & McAdoo, 1979). As the upwelling of the mantle as part of the Airy isostatic compenstation cools there will be thermal subsidence in the basin, which Turcotte and McAdoo (1979) estimates to be in the range of about 1/3 of the current basin depth.

The depth of the LA basin has been studied using various geophysical methods, including gravity measurements, seismic tomography, and receiver functions. Gravity measurements have been used to infer the density

19448007, 2024, 18, Downloaded from https://agupubs.onlinelibrary.wiley.com/doi/10.1029/2024GL111135 by University Of California, Wiley Online Library on [28/09/2024]. See the Terms and Conditions (https://onlinelibrary.wiley.com/terms-and-conditions) on Wiley Online Library for rules of use; OA articles are governed by the applicable Creative Commons License

distribution within the basin, providing insights into its composition and structure. According to McCulloh (1960), the maximum depth of the LA basin is estimated to be 9.1 km. However, this estimate carries considerable uncertainty due to the poorly known density distribution with depth (Wright, 1991). Seismic tomography studies at multiple scales have revealed complex subsurface velocity structure of the LA basin, but these results are usually insensitive to sharp discontinuities (Castellanos & Clayton, 2021; Jia & Clayton, 2021; Lee et al., 2014; Lin et al., 2013; Nakata et al., 2015). Seismic receiver function studies have been instrumental in identifying seismic discontinuities, contributing significantly to our understanding of the basin's overall shape and depth. However, these studies are typically limited to dense linear arrays in order to permit the identification of the scattered phases. Ma and Clayton (2016) is one of the few studies that provided a detailed depth estimate for the central LA basin, largely due to the limited availability of dense arrays in the basin at that time. Other receiver function studies have primarily focused on the northern LA basins, utilizing temporary dense deployments (Ghose et al., 2023; Liu et al., 2018; Wang et al., 2021) or sparse permanent stations within the Southern California Seismic Network (SCSN) to study the broader southern California region (Yan & Clayton, 2007), resulting in limited resolution for the LA basin itself. Similar to the receiver function methods, Sp converted phases from local earthquakes have been used to map basin depth (Chopra et al., 2010; Langston, 2003; Mandal, 2007). However, to our knowledge, no prior studies have specifically utilized Sp converted phases to map the entire LA basin, largely due to the challenges of identifying these phases in urban settings with sparse arrays. Consequently, a comprehensive and detailed picture of the basin's depth and structure remains elusive, primarily due to limitations in spatial coverage of seismic arrays.

The Community Seismic Network (CSN) represents significant progress in this context by providing low-cost, dense data coverage for detailed seismic hazard studies of the LA basin (Clayton et al., 2015). The CSN has been used to detect and analyze seismic events in real-time, improve models of ground motion and site amplification, and refine seismic velocity model based on ground motions (Clayton et al., 2019; Kohler et al., 2013; Muir et al., 2022). In June-July 2022, a collaborative effort by the University of Utah, Caltech, and UC Riverside, deployed a ∼300-node survey throughout the LA Basin, significantly expanding upon the 40 stations of the permanent SCSN. This dense array, known as the Los Angeles Basin 2022 (LAB2022) project, has enabled high-resolution mapping of the LA basin using multiple seismological techniques.

In this paper, we aim to leverage the two dense arrays, CSN and LAB2022, along with the SCSN, to map the LA basin's depth using Sp converted phases. All the methods we use allow the results to be easily converted to alternate velocity models with reasonable accuracy.

2. Observation and Synthetics of Sp Converted Phases

2.1. Dense Seismic Arrays and Local Earthquakes

A total of 729 stations were utilized in this study, including 41 broadband stations from SCSN, 289 nodes from LAB2022, and 399 accelerometers from CSN (Figure 1a). The CSN network consists of strong-motion accelerometers with an average interstation distance of 0.8 km, located in the Los Angeles area of California (Clayton et al., 2015). The noise floor of these accelerometers is higher than the ambient noise level and consequently cannot be used for ambient noise interferometry, however, they can still record clear waveforms for local earthquakes of magnitude 3.5 or greater. LAB2022 includes two linear arrays with about 48 nodes each and approximately 200 additional stations distributed across the basin, providing dense coverage (Figure 1a). This dense coverage is essential for capturing and identifying coherent arrivals of the Sp phases that help in mapping subsurface structures with high resolution.

The first event with a visible Sp phase between P and S phases was the M3.5 Compton event in October 2019 (Figure 1b). The hypocenter depth of this event, according to the SCSN catalog, is 23.6 km, which is well below the basin and very close to, if not below, the Moho depth in this region. After reviewing all M3+ events recorded by the CSN during its operation, we identified four events with clearly visible Sp phases. Additionally, during the one-month deployment of LAB2022, we observed five events with magnitudes around 2 and depths approaching or exceeding 10 km that also exhibited clear Sp phases. Detailed information about these events is provided in Table S1 in Supporting Information S1.

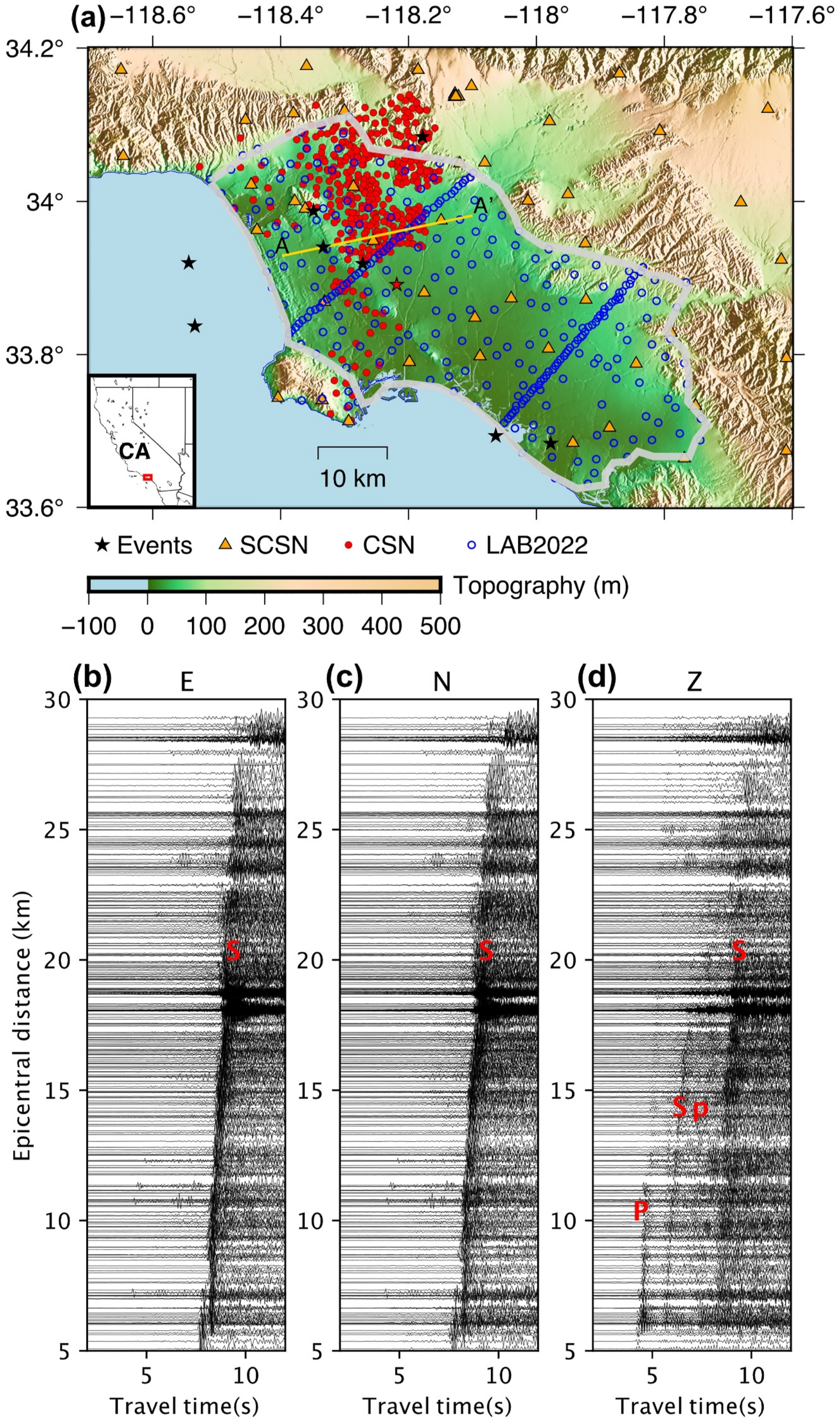

Figure 1. Geological setting and waveform data. (a) Map of stations and event epicenters used in this study. The LA basin is outlined by the gray line. Red dots represent CSN sensors, blue circles denote the LAB2022 node array, and orange triangles indicate SCSN stations. Black stars mark the epicenters of the events analyzed in this study, with the October 2019 Compton event highlighted by a red star. The AA' line shows the location of the simulation profile depicted in Figure 2 and Video S1. (b) Three-component waveform recorded during the October 2019 Compton event, displaying a clear Sp phase on the vertical component only.

19448007, 2024, 18, Downloaded from https://agupubs.onlinelibrary.wiley.com/doi/10.1029/2024GL111135 by University Of California, Wiley Online Library on [28/09/2024]. See the Terms and Conditions (https://onlinelibrary.wiley.com/terms-and-conditions) on Wiley Online Library for rules of use; OA articles are governed by the applicable Creative Commons License

19448007, 2024, 18, Downloaded from https://agupubs.onlinelibrary.wiley.com/doi/10.1029/2024GL111135 by University Of California, Wiley Online Library on [28/09/2024]. See the Terms and Conditions (https://onlinelibrary.wiley.com/terms-and-conditions) on Wiley Online Library for rules of use; OA articles are governed by the applicable Creative Commons License

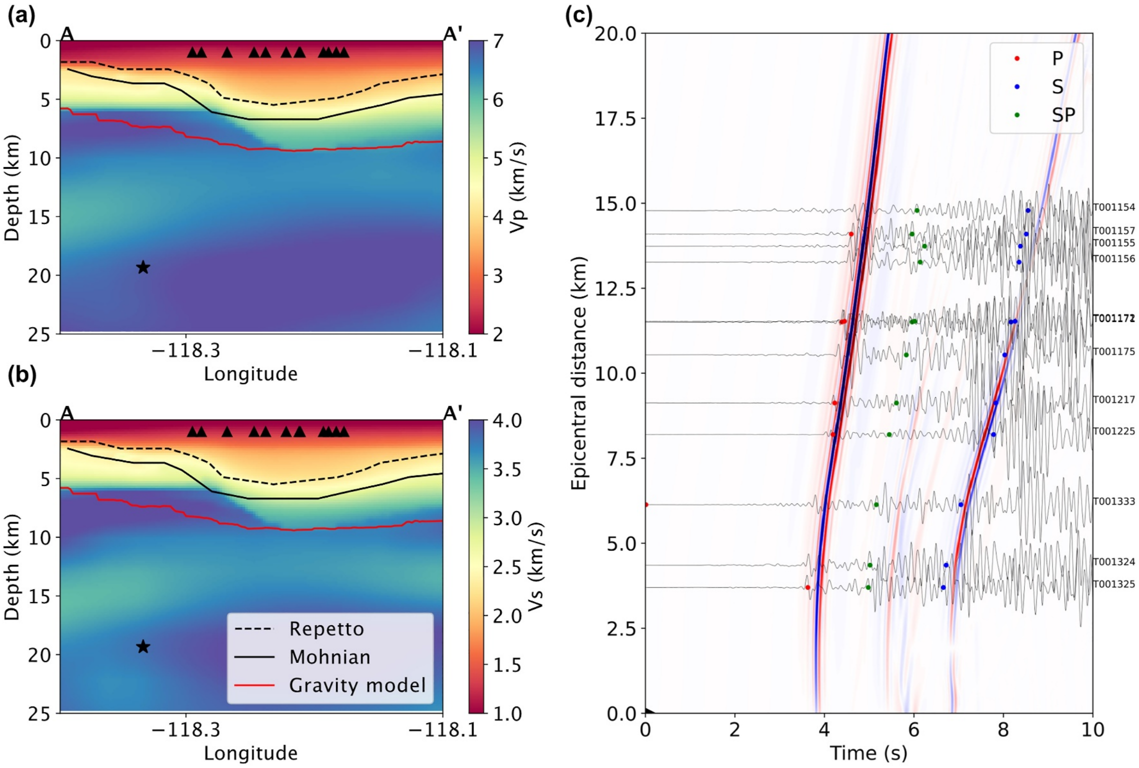

Figure 2. Wavefield simulation and observation of the M4.0 earthquake on 05 April 2021. (a) The P-velocity model along the profile AA’ (Figure 1a) sliced from CVM-SCEC 4.26. The event hypocenter and the stations within 1 km from the profile are plotted as a star and triangles, respectively. The two geological boundaries between different types of sedimentary rock layers within the LA basin, Repetto and Mohnian interfaces, are plotted with dashed and solid lines, respectively. (b) Similar to (a), but for the S-velocity model. (c) The background image shows the vertical component wavefield simulation on the surface receivers, with clearly visible P, Sp, and S phases. The black waveform shows the observed data. The red and blue dots are P and S arrival picks from PhaseNet. The green dots are manual picks of Sp phases.

2.2. Observation and Synthetics of the Local Earthquakes

Clear arrivals between the P and S phases are visible only on the vertical component (Figure 1d). We use PhaseNet to pick the P and S arrival times of these events based on three-component data (Zhu & Beroza, 2019). PhaseNet is a neural network-based picker that improves the accuracy and consistency of phase picking, which is essential for reliable phase identification and subsequent analysis. PhaseNet is trained to only pick the P and S waves, and hence we manually pick the arrival times of the Sp phases (Figure 2c). Since the Sp phase is only visible in the vertical component, we considered several candidates for this phase ending with the P wave to the surface: basin and surface reflected P wave (PpPp), basin converted P wave (Sp), and Moho reflected P wave (PmP).

Further verification was conducted using 2D full waveform modeling with the community velocity model CVM-SCEC 4.26 (Figure 2ab) (Lee et al., 2014; Li et al., 2014; Small et al., 2017). This 3D model is derived from full-waveform tomography, making it a best model for simulating seismic wave propagation. Supplementary Video S1 demonstrates that the observed intermediate phase corresponds to an Sp wave converted at the basin interface. Comparing the observed waveforms and phase picks with the synthetic seismograms, we found good alignment of the P and S arrivals. However, the Sp observed arrival time is consistently earlier than the synthetic arrival time (Figure 2c), suggesting that the phase is converted at a deeper interface, indicating that the basin might be deeper than currently modeled by the community velocity model. This discrepancy highlights the need for updating the model with more accurate basin depths.

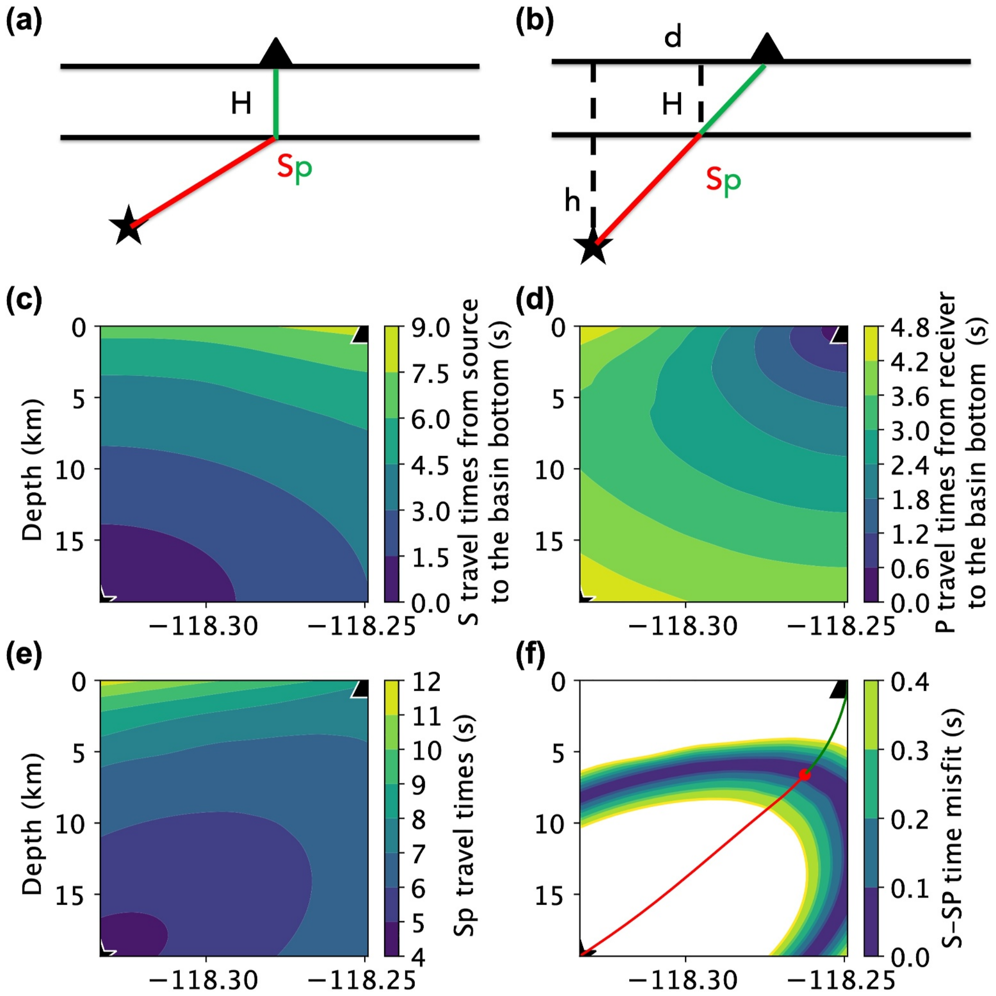

Figure 3. Illustration of three different mapping schemes. (a) Mapping basin depth assuming the Sp path is vertically incident in the basin. (b) Mapping basin depth assuming the Sp path follows a straight trajectory from source to receiver. (c) S-wave travel times from the source to potential conversion points at basin bottom computed using ray tracing. (d) P-wave travel times from the receiver to potential conversion points at basin bottom computed using ray tracing. (e) Sp converted arrival times from source to receiver, derived by adding the travel times from (c) and (d). (f) The area where travel times differ by more than 0.4 s from the observed Sp travel time is masked. The final raypath is determined by conserving horizontal slowness.

3. Mapping LA Basin Depth

With phase picks of P, S, and Sp converted arrivals, we can use the differential travel times of these phases to map the LA basin depth. We apply three approaches, ranging from simple to complex, to estimate the basin depth.

3.1. Conventional Mapping Method

The first approach is the conventional method for mapping basin depth using converted phases, which assumes a vertically incident plane wave for the Sp phase (Bao et al., 2021; Chopra et al., 2010; Mandal, 2007; Stone et al., 2021):

$$H = \frac{T_{Ss-Sp}}{\frac{1}{V_S} - \frac{1}{V_P}} \tag{1}$$

Where V_P,V_S represent the time-averaged velocities of P and S waves in the basin, respectively, $T_{Ss\text{-}Sp}$ is the differential travel time between the Sp converted wave and the S wave, and H represents the basin depth

19448007, 2024, 18, Downloaded from https://agupubs.onlinelibrary.wiley.com/doi/10.1029/2024GL111135 by University Of California, Wiley Online Library on [28/09/2024]. See the Terms and Conditions (https://onlinelibrary.wiley.com/terms-and-conditions) on Wiley Online Library for rules of use; OA articles are governed by the applicable Creative Commons License

(Figure 3a). With a known reference velocity model, we can calculate the time-averaged velocities and, by assuming a uniform V_P within the basin and V_S below the basin, estimate the basin depth using the measured differential travel times. This simplified approach, which is commonly used in receiver functions, is generally effective for mapping relatively shallow basins with depths of 1–2 km and with earthquakes far away, where the basin structure constitutes only a small fraction of the entire wave path from source to receiver. In such scenarios, the assumption of a vertically incident Sp wave near the station holds. This method has been validated in several Sp phase studies (Bao et al., 2021; Chopra et al., 2010; Mandal, 2007; Stone et al., 2021), demonstrating its effectiveness in various geological settings.

3.2. Modified Conventional Method

In our case, where the epicentral distances are comparable to the event depths, the entire raypath becomes intertwined with the basin structure of interest. To address this complexity, we modify the assumption of a vertically incident Sp phase. Based on CVM-SCEC 4.26, the depth-averaged V_P in the basin is only slightly larger than the V_S in the lower crust, suggesting that the raypath is generally straight from the hypocenter to the station (Figure 3b). The basin depth at the conversion point can be calculated as:

$$H = \frac{T_{Ss-Sp}}{\frac{1}{V_S} - \frac{1}{V_P}} \cdot \frac{h}{\sqrt{h^2 + d^2}} \tag{2}$$

where h is the hypocenter depth, and d is the epicentral distance. This adjustment moves the conversion point toward the epicenter (Figure 3b).

3.3. Detailed Ray-Tracing Analysis

The next level of complexity is to use ray tracing to more precisely calculate the ray paths of Sp and S waves. This method allows us to model the travel paths of seismic waves through a heterogeneous medium, taking into account seismic velocities both within and below the basin. We use the PyKonal package, which leverages a fast marching algorithm to efficiently solve the Eikonal equation (White et al., 2020). For each event-station pair, we calculate the S wave travel time from the event location (Figure 3c) and the P wave travel time from the station location (Figure 3d). By overlaying these travel time plots, we can identify the Sp travel times converted at various points within the event-station plane (Figure 3e). Note that we performed 2D ray tracing in the event-station plane rather than 3D ray tracing. This approach significantly reduces computational demands and narrows the range of candidate conversion points to search over. This simplification is valid because most of the ray paths lie within the event-station plane, and the difference between 2D ray tracing and 3D ray tracing is minimal (Figure S1 in Supporting Information S1). To pinpoint the actual conversion points, we apply Snell's law, ensuring that the horizontal slowness is conserved along the raypath assuming the boundary is locally horizonal at the conversion point. By calculating the horizontal slowness at each grid point along the raypath, we can accurately identify the most plausible conversion points (Figure 3f).

4. Results

We mapped the LA basin depth using all three methods described above. For the first two methods, we need to use the average V_P and V_S in the basin. We use the model from Muir et al. (2022), in which the basin bottom and the velocity model are both defined. The time averaged V_P and V_S in the basin are 3.602 km/s and 1.880 km/s, respectively. The basin depth mapped using the vertically incident Sp phase method (Figure 4a) fails to produce a clearly visible basin depth pattern, with the mapped depth consistently exceeding 8 km, especially in the southeastern part of the LA Basin, which is unreasonable. The uncertainty, computed as the standard deviation of all measurements within each grid, is presented in Figure 4b. This method shows high uncertainty across the entire basin, with an average standard deviation of 3.14 km.

The basin depth mapped using the straight trajectory method is shown in Figure 4c. This approach provides a more reasonable and detailed basin pattern, improving both depth estimation and spatial resolution compared to the conventional method. The uncertainty for this method is shown in Figure 4d, with an average standard deviation of only 0.59 km. This reduced uncertainty makes the modified straight trajectory method a simpler yet more reliable option for mapping LA basin depth.

19448007, 2024, 18, Downloaded from https://agupubs.onlinelibrary.wiley.com/doi/10.1029/2024GL111135 by University Of California, Wiley Online Library on [28/09/2024]. See the Terms and Conditions (https://onlinelibrary.wiley.com/terms-and-conditions) on Wiley Online Library for rules of use; OA articles are governed by the applicable Creative Commons License

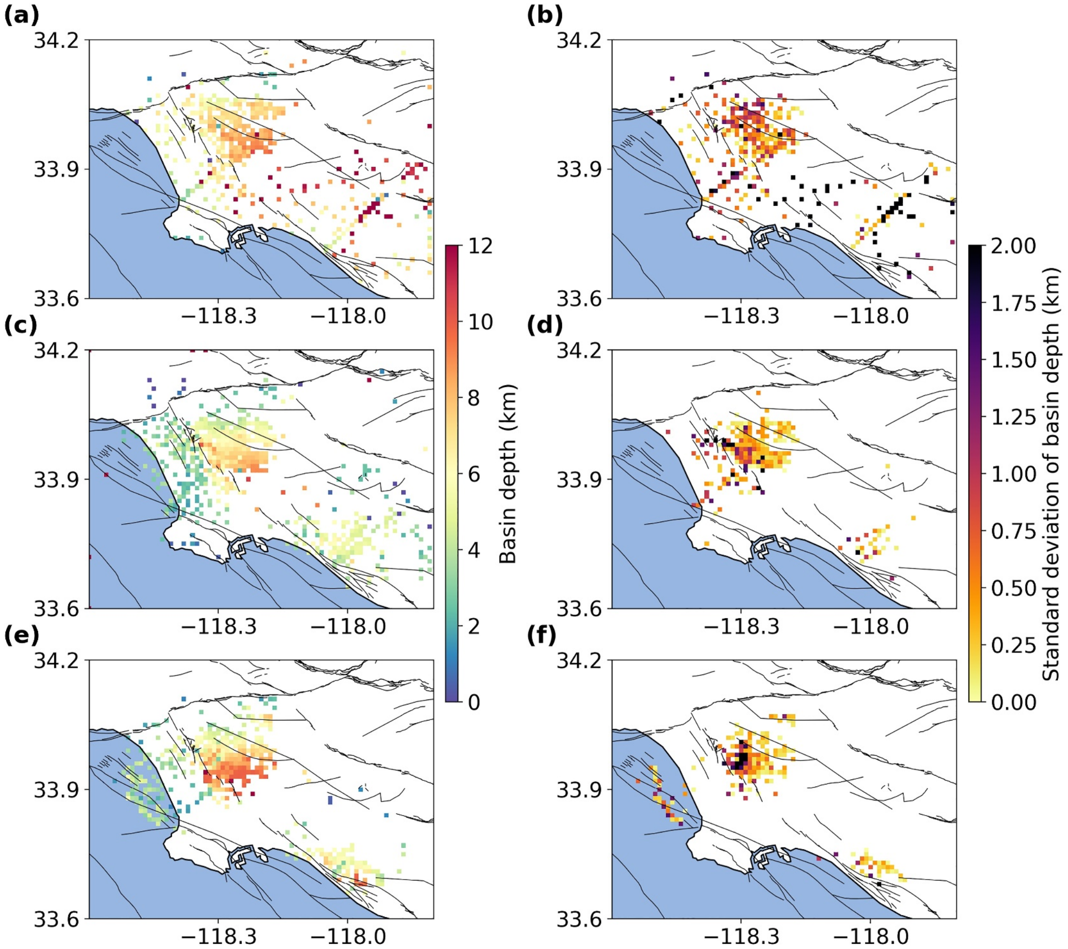

Figure 4. LA basin mapping results. The results are mapped onto a mesh and averaged across all available station-event pairs. (a) Mapped depth using the conventional method illustrated in Figure 3a. (b) The uncertainty, computed as the standard deviation of all measurements within each grid (if more than one measurement is available). (c) Mapped depth using the straight-trajectory method illustrated in Figure 3b. (d) Uncertainty corresponding to (c), computed as the standard deviation of all measurements within each grid. (e) Mapped depth using the detailed ray-tracing method illustrated in Figures 3c–3f. (f) Uncertainty corresponding to (e), computed as the standard deviation of all measurements within each grid.

The basin depth using the detailed ray-tracing method is presented in Figure 4e. The reference velocity model is the CVM-SCEC 4.26 (Lee et al., 2014). This method shows a basin pattern generally consistent with the one in Figure 4c, but the use of a detailed velocity model allows for refined mapping for each individual event-station pair, resulting in a slightly deeper depth. The uncertainty for the detailed ray-tracing method is shown in Figure 4f, with an average standard deviation of 0.56 km, making it a slightly more robust result. Here, we averaged the velocity model in the event-station plane to reduce the effect of local heterogeneities in the 3D velocity model, which is not perfect. Using the 3D velocity model directly increases the average uncertainty to 0.72 km (Figure S2 in Supporting Information S1).

The second and third methods produce more reasonable basin patterns and lower uncertainties than the conventional method. The deepest part of the LA basin in the Central Basin has an average depth of 9.2 km, with a sharp increase in depth observed on the north side of the NIF. The simplicity of the straight-ray method and its variance reduction comparable to the ray-tracing method (0.59 vs. 0.56), makes it a very useful method to switch between velocity models.

19448007, 2024, 18, Downloaded from https://agupubs.onlinelibrary.wiley.com/doi/10.1029/2024GL111135 by University Of California, Wiley Online Library on [28/09/2024]. See the Terms and Conditions (https://onlinelibrary.wiley.com/terms-and-conditions) on Wiley Online Library for rules of use; OA articles are governed by the applicable Creative Commons License

19448007, 2024, 18, Downloaded from https://agupubs.onlinelibrary.wiley.com/doi/10.1029/2024GL111135 by University Of California, Wiley Online Library on [28/09/2024]. See the Terms and Conditions (https://onlinelibrary.wiley.com/terms-and-conditions) on Wiley Online Library for rules of use; OA articles are governed by the applicable Creative Commons License

5. Discussion and Conclusion

5.1. Implications of Results

Having an accurate estimate of the basin depth and shape is important for two reasons. The first is that the resonance properties for earthquake strong motions primary depends on the local depth of the basin, its shape and the shear wave velocities. The calculation of the resonace spectrum of the basin is complicated (Rial, 1989), but with a 1D approximation it is 12 s, with the first overtone at 4 s. This is in the range of the fundamental mode of a 50-floor building (5 s). The site amplification pattern observed during the 2019 M7 Ridgecrest earthquake, as reported by Filippitzis et al. (2021) and Kohler et al. (2020) was spatially correlated with our mapped basin depth at periods of 1–12 s. This highlights the critical importance of considering basin depth when designing tall buildings in Los Angeles to mitigate potential seismic risks. Additionally, other factors such as basin-edge effects and wave focusing due to basin boundary curvatures also play significant roles in amplifying ground motions and can be better characterized with these dense arrays used in this study.

The basin depths are also important for investigating the tectonics of the area. The free-air gravity over the LA Basin is approximately −50 mgal, which when compared to a −300 mgal that is due to the basin itself (Turcotte & McAdoo, 1979), indicates that the basin very close to isostatic equilibrium. Assuming an Airy mechanism, this means that the Moho in this area is upwarped by an amount approximately equal to the basin depth. This was directly observed by Ma and Clayton (2016) on a line across the southern LA Basin. Assuming an average Moho depth in the Los Angeles region, it means that the original crust beneath LA is thinned to as little as 6 km. This thinning is created by (at least) two factors: the first is the stretching due to the opening of the accommodation space in the wake of the rotation of the Transverse Ranges, and the second is the thermal subsidence that occurs when the upwelling mantle that provides the isostatic compensation cools. Ma and Clayton (2016) directly observe and estimate the basin depth and the Moho depth, and hence they can estimate the stretching factor of the to be approximately 2. This means that the thermal contraction component of the basin depth is about 3 km (Turcotte & McAdoo, 1979).

5.2. Methodological Insights

We extend methods for mapping the LA basin depth using Sp phases from local earthquakes recorded by dense arrays. The ray-tracing method, which accounts for most wave propagation complexities, offers the highest accuracy and lowest uncertainty. However, it is highly dependent on the geometry of the existing basin boundaries within the reference model, making the velocity model the primary source of uncertainty. Regular updates to the velocity model will naturally enhance the accuracy of basin depth mapping. In contrast, the straight-line raypath approach is a simplified modification of the conventional method that acknowledges the intertwined nature of the source location and wave propagation problem with the velocity model. Despite its simplicity, this method effectively captures key aspects of wave propagation and provides valuable first-order estimates of basin depth that are less dependent on specific details of the velocity model.

In Figure 5, we show the basin depth of a cross-section across the NIF. In Figure 5b, we show results mapped with the method in Figure 3b using average basin velocity derived from different reference models. The basin depths calculated using the model in Muir et al. (2022) and that in the CVM-Harvard model (Shaw et al., 2015) are consistent, but about 2 km above the depth derived using CVM-SCEC model (Lee et al., 2014). In Figure 5c, the basin depth derived using ray tracing of CVM-SCEC model is slightly deeper than previous models but is quite consistent with that using straight ray assumption and the same velocity model.

Thanks to the dense coverage provided by the permanently monitoring CSN, we will continue to receive additional data, improving the resolution and coverage of the LA basin depth mapping. With more data, it will be important to develop automatic algorithms for Sp phase picking. Our current manual picks may serve as labels for training these algorithms.

5.3. Conclusions

The depth of the LA basin has been accurately mapped using two dense seismic arrays: the CSN and the LAB2022. These arrays allow us to identify Sp converted phases from local earthquakes and utilize differential travel times between direct S waves and Sp converted phases to map the basin depth. This mapping offers independent constraints that complement previous seismic tomography and gravity surveys. The results indicate

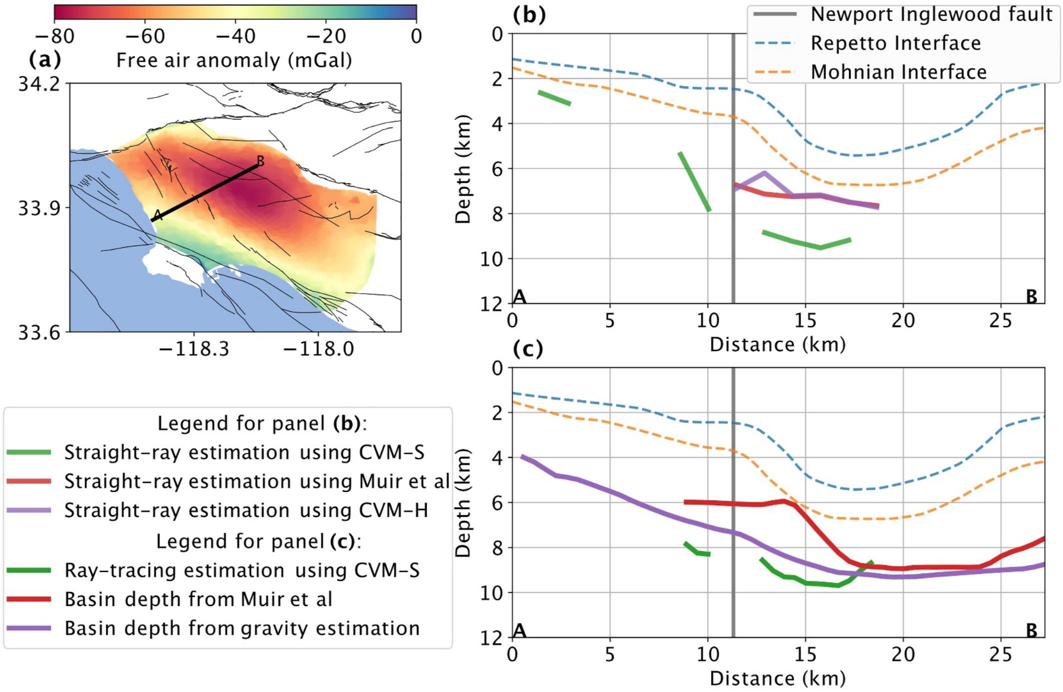

Figure 5. Comparison among cross-sections of different basin depth models. (a) Free-air gravity anomaly in the LA basin and the location of cross-section AB across the NIF. (b) The basin depth mapped using the straight-trajectory method with average basin velocity from different reference velocity models are plotted in solid lines. The Repetto and Mohnian interfaces are plotted with dashed lines. The intersection of the NIF with the cross-section is indicated by the vertical gray lines. (c) The purple line represents the gravity-derived basin depth. The red line shows the basin depth from Muir et al. (2022). The basin depth mapped using the ray tracing methods is shown by the green line.

that a substantial part of the central LA Basin has a depth of over 9 km, which enhances our understanding of the basin's geological structure and contributes to better seismic hazard assessments.

Data Availability Statement

The event data used in the research are all publicly available on CSN website (http://csn.caltech.edu/data/). The depth model and phase picks are made publicly available at Yang (2024). These will allow the results to be converted to any velocity model and allow new events to be added.

Acknowledgments
The authors thank the LAB2022 deployment team who make all the field work. The authors thank helpful discussion with Qiushi Zhai, Weiqiang Zhu, and Ettore Biondi. The authors thank Valeria Villa for providing digitalized maps of Repetto and Mohnian interfaces. This research was funded by the Southern California Earthquake Center (SCEC) award 22019.

References

Bao, F., Li, Z., Shi, Y., Tian, B., Chong, J., & Rong, W. (2021). Sediment structures constrained by converted waves from local earthquakes recorded by a dense seismic array in the Tangshan earthquake region. *Pure and Applied Geophysics*, *178*(2), 379–397. https://doi.org/10.1007/s00024-021-02667-5

Castellanos, J. C., & Clayton, R. W. (2021). The fine-scale structure of long beach, California, and its impact on ground motion acceleration. *Journal of Geophysical Research: Solid Earth*, *126*(12). https://doi.org/10.1029/2021jb022462

Chopra, S., Rao, K. M., & Rastogi, B. K. (2010). Estimation of sedimentary thickness in Kachchh basin, Gujarat using SP converted phase. *Pure and Applied Geophysics*, *167*(10), 1247–1257. https://doi.org/10.1007/s00024-009-0022-3

Clayton, R. W., Heaton, T., Kohler, M., Chandy, M., Guy, R., & Bunn, J. (2015). Community seismic network: A dense array to sense earthquake strong motion. *Seismological Research Letters*, *86*(5), 1354–1363. https://doi.org/10.1785/0220150094

Clayton, R. W., Kohler, M., Guy, R., Bunn, J., Heaton, T., & Chandy, M. (2019). CSN-LAUSD network: A dense accelerometer network in Los Angeles schools. *Seismological Research Letters*, *91*(2A), 622–630. https://doi.org/10.1785/0220190200

Denolle, M. A., Dunham, E. M., Prieto, G. A., & Beroza, G. C. (2014). Strong ground motion prediction using virtual earthquakes. *Science*, *343*(6169), 399–403. https://doi.org/10.1126/science.1245678

Filippitzis, F., Kohler, M. D., Heaton, T. H., Graves, R. W., Clayton, R. W., Guy, R. G., et al. (2021). Ground motions in urban Los Angeles from the 2019 Ridgecrest earthquake sequence. *Earthquake Spectra*, *37*(4), 2493–2522. https://doi.org/10.1177/87552930211003916

Ghose, R., Persaud, P., & Clayton, R. W. (2023). Basin structure for earthquake ground motion estimates in urban Los Angeles mapped with nodal receiver functions. *Geosciences*, *13*(11), 320. https://doi.org/10.3390/geosciences13110320

Hough, S. E., & Graves, R. W. (2020). The 1933 long beach earthquake (California, USA): Ground motions and rupture scenario. *Scientific Reports*, *10*(1), 10017. https://doi.org/10.1038/s41598-020-66299-w

19448007, 2024, 18, Downloaded from https://agupubs.onlinelibrary.wiley.com/doi/10.1029/2024GL111135 by University Of California, Wiley Online Library on [28/09/2024]. See the Terms and Conditions (https://onlinelibrary.wiley.com/terms-and-conditions) on Wiley Online Library for rules of use; OA articles are governed by the applicable Creative Commons License

Ingersoll, R. V., & Rumelhart, P. E. (1999). Three-stage evolution of the Los Angeles basin, southern California. *Geology*, *27*(7), 593. https://doi.org/10.1130/0091-7613(1999)027<0593:TSEOTL>2.3.CO;2

Jia, Z., & Clayton, R. W. (2021). Determination of near surface shear-wave velocities in the central Los Angeles basin with dense arrays. *Journal of Geophysical Research: Solid Earth*, *126*(5), e2020JB021369. https://doi.org/10.1029/2020JB021369

Kohler, M. D., Filippitzis, F., Heaton, T., Clayton, R. W., Guy, R., Bunn, J., & Chandy, K. M. (2020). 2019 ridgecrest earthquake reveals areas of Los Angeles that amplify shaking of high-rises. *Seismological Research Letters*, *91*(6), 3370–3380. https://doi.org/10.1785/0220200170

Kohler, M. D., Heaton, T. H., & Cheng, M.-H. (2013). (Vol. *8692*, pp. 1049–1056). The Community Seismic Network and Quake-Catcher Network: Enabling structural health monitoring through instrumentation by community participants. *Sensors and Smart Structures Technologies for Civil, Mechanical, and Aerospace Systems 2013*.

Langston, C. A. (2003). Local earthquake wave propagation through Mississippi embayment sediments, Part I: Body-wave phases and local site responses. *Bulletin of the Seismological Society of America*, *93*(6), 2664–2684. https://doi.org/10.1785/0120030046

Lee, E. J., Chen, P., Jordan, T. H., Maechling, P. B., Denolle, M. A. M., & Beroza, G. C. (2014). Full-3-D tomography for crustal structure in Southern California based on the scattering-integral and the adjoint-wavefield methods. *Journal of Geophysical Research: Solid Earth*, *119*(8), 6421–6451. https://doi.org/10.1002/2014JB011346

Li, D., Helmberger, D., Clayton, R. W., & Sun, D. (2014). Global synthetic seismograms using a 2-D finite-difference method. *Geophysical Journal International*, *197*(2), 1166–1183. https://doi.org/10.1093/gji/ggu050

Lin, F. C., Li, D., Clayton, R. W., & Hollis, D. (2013). High-resolution 3D shallow crustal structure in Long Beach, California: Application of ambient noise tomography on a dense seismic array. *Geophysics*, *78*(4), Q45–Q56. https://doi.org/10.1190/geo2012-0453.1

Liu, G., Persaud, P., & Clayton, R. W. (2018). Structure of the northern Los Angeles basins revealed in teleseismic receiver functions from short-term nodal seismic arrays. *Seismological Research Letters*, *89*(5), 1680–1689. https://doi.org/10.1785/0220180071

Ma, Y., & Clayton, R. W. (2016). Structure of the Los Angeles Basin from ambient noise and receiver functions. *Geophysical Journal International*, *206*(3), 1645–1651. https://doi.org/10.1093/gji/ggw236

Mandal, P. (2007). Sediment thicknesses and Qs vs. Qp Relations in the Kachchh rift basin, Gujarat, India using Sp converted phases. *Pure and Applied Geophysics*, *164*(1), 135–160. https://doi.org/10.1007/s00024-006-0158-3

McCulloh, T. H. (1960). Gravity variations and the geology of the Los Angeles basin of California. *US Geol. Surv. Profess. Pap.*, *400-B*, 320–325.

McKenzie, D. (1978). Some remarks on the development of sedimentary basins. *Earth and Planetary Science Letters*, *40*(1), 25–32. https://doi.org/10.1016/0012-821X(78)90071-7

Muir, J. B., Clayton, R. W., Tsai, V. C., & Brissaud, Q. (2022). Parsimonious velocity inversion applied to the Los Angeles basin, CA. *Journal of Geophysical Research: Solid Earth*, *127*(2). https://doi.org/10.1029/2021JB023103

Nakata, N., Chang, J. P., Lawrence, J. F., & Boué, P. (2015). Body wave extraction and tomography at Long Beach, California, with ambient-noise interferometry. *Journal of Geophysical Research: Solid Earth*, *120*(2), 1159–1173. https://doi.org/10.1002/2015JB011870

Olsen, K. B. (2000). Site amplification in the Los Angeles basin from three-dimensional modeling of ground motion. *Bulletin of the Seismological Society of America*, *90*(6B), S77–S94. https://doi.org/10.1785/0120000506

Rial, J. A. (1989). Seismic wave resonances in 3-D sedimentary basins. *Geophysical Journal International*, *99*(1), 81–90. https://doi.org/10.1111/j.1365-246X.1989.tb02016.x

Shaw, J. H., Plesch, A., Tape, C., Suess, M. P., Jordan, T. H., Ely, G., et al. (2015). Unified Structural Representation of the southern California crust and upper mantle. *Earth and Planetary Science Letters*, *415*, 1–15. https://doi.org/10.1016/j.epsl.2015.01.016

Shaw, J. H., & Suppe, J. (1996). Earthquake hazards of active blind-thrust faults under the central Los Angeles basin, California. *Journal of Geophysical Research*, *101*(B4), 8623–8642. https://doi.org/10.1029/95JB03453

Small, P., Gill, D., Maechling, P. J., Taborda, R., Callaghan, S., Jordan, T. H., et al. (2017). The SCEC unified community velocity model software framework. *Seismological Research Letters*, *88*(6), 1539–1552. https://doi.org/10.1785/0220170082

Stone, I., Wirth, E. A., & Frankel, A. D. (2021). Structure and QP–QS relations in the Seattle and Tualatin basins from converted seismic phases. *Bulletin of the Seismological Society of America*, *111*(3), 1221–1233. https://doi.org/10.1785/0120200390

Turcotte, D. L., & McAdoo, D. C. (1979). Thermal subsidence and petroleum generation in the southwestern block of the Los Angeles Basin, California. *Journal of Geophysical Research*, *84*(B7), 3460–3464. https://doi.org/10.1029/JB084iB07p03460

Wang, X., Zhan, Z., Zhong, M., Persaud, P., & Clayton, R. W. (2021). Urban Basin structure imaging based on dense arrays and Bayesian array-based coherent receiver functions. *Journal of Geophysical Research: Solid Earth*, *126*(9), e2021JB022279. https://doi.org/10.1029/2021JB022279

White, M. C. A., Fang, H., Nakata, N., & Ben-Zion, Y. (2020). PyKonal: A Python package for solving the Eikonal equation in spherical and Cartesian coordinates using the fast marching method. *Seismological Research Letters*, *91*(4), 2378–2389. https://doi.org/10.1785/0220190318

Wright, T. L. (1991). *Structural geology and tectonic evolution of the Los Angeles Basin, California* (pp. 35–134). Active Margin Basins.

Yan, Z., & Clayton, R. W. (2007). Regional mapping of the crustal structure in southern California from receiver functions. *Journal of Geophysical Research*, *112*(B5). https://doi.org/10.1029/2006JB004622

Yang, Y. (2024). Event catalog, Sp phase picks, and mapped Los Angels basin depth. [Dataset]. *Zenodo*. https://doi.org/10.5281/zenodo.12602047

Yerkes, R. F. (1965). *Geology of the Los Angeles basin, California: An introduction*. US Government Printing Office.

Zhu, W., & Beroza, G. C. (2019). PhaseNet: A deep-neural-network-based seismic arrival-time picking method. *Geophysical Journal International*, *216*(1), 261–273. https://doi.org/10.1093/gji/ggy423

19448007, 2024, 18, Downloaded from https://agupubs.onlinelibrary.wiley.com/doi/10.1029/2024GL111135 by University Of California, Wiley Online Library on [28/09/2024]. See the Terms and Conditions (https://onlinelibrary.wiley.com/terms-and-conditions) on Wiley Online Library for rules of use; OA articles are governed by the applicable Creative Commons License